

VU Research Portal

Extreme mechanics of colloidal polymers under compression: Buckling, creep, and break-up

Stuij, Simon G.; Biebricher, Andreas; Gong, Zhe; Sacanna, Stefano; Peterman, Erwin; Heller, Iddo; Schall, Peter

published in

PHYSICAL REVIEW MATERIALS
2022

DOI (link to publisher)

[10.1103/PhysRevMaterials.6.035603](https://doi.org/10.1103/PhysRevMaterials.6.035603)

document version

Publisher's PDF, also known as Version of record

document license

Article 25fa Dutch Copyright Act

[Link to publication in VU Research Portal](#)

citation for published version (APA)

Stuij, S. G., Biebricher, A., Gong, Z., Sacanna, S., Peterman, E., Heller, I., & Schall, P. (2022). Extreme mechanics of colloidal polymers under compression: Buckling, creep, and break-up. *PHYSICAL REVIEW MATERIALS*, 6(3), 1-9. [035603]. <https://doi.org/10.1103/PhysRevMaterials.6.035603>

General rights

Copyright and moral rights for the publications made accessible in the public portal are retained by the authors and/or other copyright owners and it is a condition of accessing publications that users recognise and abide by the legal requirements associated with these rights.







- Users may download and print one copy of any publication from the public portal for the purpose of private study or research.
- You may not further distribute the material or use it for any profit-making activity or commercial gain
- You may freely distribute the URL identifying the publication in the public portal ?

Take down policy

If you believe that this document breaches copyright please contact us providing details, and we will remove access to the work immediately and investigate your claim.

E-mail address:

vuresearchportal.ub@vu.nl

Extreme mechanics of colloidal polymers under compression: Buckling, creep, and break-upSimon G. Stuij ¹, Andreas Biebricher,² Zhe Gong ³, Stefano Sacanna ³, Erwin Peterman ²,
Iddo Heller ² and Peter Schall ¹¹*Institute of Physics, University of Amsterdam, Science Park 904, 1098 XH Amsterdam, the Netherlands*²*Department of Physics and Astronomy and LaserLaB, Vrije Universiteit, Amsterdam, the Netherlands*³*Molecular Design Institute, Department of Chemistry, New York University, 29 Washington Place, New York 10003, USA*

(Received 22 July 2021; accepted 2 February 2022; published 25 March 2022)

Self-assembling patchy colloidal particles form a promising platform to create designer soft materials. To dress such systems with mechanical functionality, one can take inspiration from biological structures such as the cell's cytoskeleton, which consists of semiflexible filaments, whose mechanical behavior give the cell its unique mechanical properties. Here we present mechanical experiments on analogs of biological fibers, semiflexible “colloidal polymers” made from bonded patchy colloidal particles. We use optical tweezers to probe their extreme mechanics under increasingly high compressions and we reveal a rich nonlinear mechanical response involving buckling, viscoelastic creep, and ultimately break-up. We characterize and model this response using elastic and viscoelastic models involving Euler buckling and stress relaxation. This allows us to identify the critical Euler buckling force, and relate the critical bending at break-up to the finite patch size of the colloids. These results demonstrate the crucial role of the patch-patch interactions in the mechanics of self-assembled colloidal materials, and they provide mechanical relationships that are essential to design functional colloidal architectures inspired by nature.

DOI: [10.1103/PhysRevMaterials.6.035603](https://doi.org/10.1103/PhysRevMaterials.6.035603)**I. INTRODUCTION**

Micrometer-sized slender structures are an integral part of many soft and biological materials. They harbor rich mechanical behavior that crucially determines the mechanical response and functionality of these soft architectures. For instance, biological filaments such as microtubules, actin filaments, and fibrin fibers, making up the cell cytoskeleton and the extracellular matrix, exhibit nonlinear buckling instabilities [1–4], viscoelastic behavior [5–8], and fracture [9,10]. Likewise, slender colloidal strands, prevalent in colloidal gels [11] and in recent colloidal designer structures [12,13], are subject to a similarly diverse mechanical response [14,15]. Such colloidal structures are easier to observe and have more controllable interparticle interactions than their biological counterparts. This makes them excellent model systems and a promising platform for designer materials with controlled internal architecture and tunable physical properties [16]. Self-assembling patchy particles, which have tunable anisotropic interactions, are a particularly promising route to achieve such designer architectures and mimic the functionalities of biological matter [17,18]. However, detailed mechanical studies of such patchy structures are still lacking. In particular, their nonlinear extreme mechanics has so far been poorly explored. For biopolymers such as microtubules and actin filaments, optical tweezers have been used to interrogate their mechanical response. To this end, microparticles are attached to the extremities of a filament, and the filament is deformed by extending or compressing it, while the tension on the filament is monitored [2,19,20]. In this way, flexural rigidity (which depends on Young's modulus and

the second moment of inertia), persistence length, and buckling forces can be measured. Typical single-filament response upon compression shows an elastic resistance followed by a compliance after buckling [21], which in the case of actin bundles is accompanied by viscoelastic relaxation [7], and fracture for extreme bending in the case of microtubules [10]. Such behavior is not limited to single filaments; rheological measurements of networks show that filaments buckle, bend, and break as a response to compression and shear, all of which contribute importantly to the nonlinear mechanics of fibrin networks [4] and microtubules [9]. Micromanipulation experiments on patchy particle assemblies, whose interactions can be controlled, would provide analogous insight into some of the principles behind the nonlinear mechanical response of colloidal architectures, with the advantage that they can be observed at the particle scale.

Here, we perform compression tests on assembled patchy particles using optical tweezers to probe their mechanics under extreme deformations. We focus on dipatch colloidal particles that self-assemble into colloidal chains via temperature-controlled critical Casimir interactions [22]. We showed previously that the resulting assembled colloidal polymers subjected to thermal noise show a two-step viscoelastic relaxation process similar to biological filaments [23]. Here, by using steady compression and creep tests on these polymers, we reveal a surprisingly complex nonlinear mechanical response resembling the richness of biological filaments, involving buckling, viscoelastic effects, and ultimately break-up upon a critical bending deformation. We characterize and model the elastic buckling and viscoelastic response and quantitatively relate the break-up point to the patch size. These

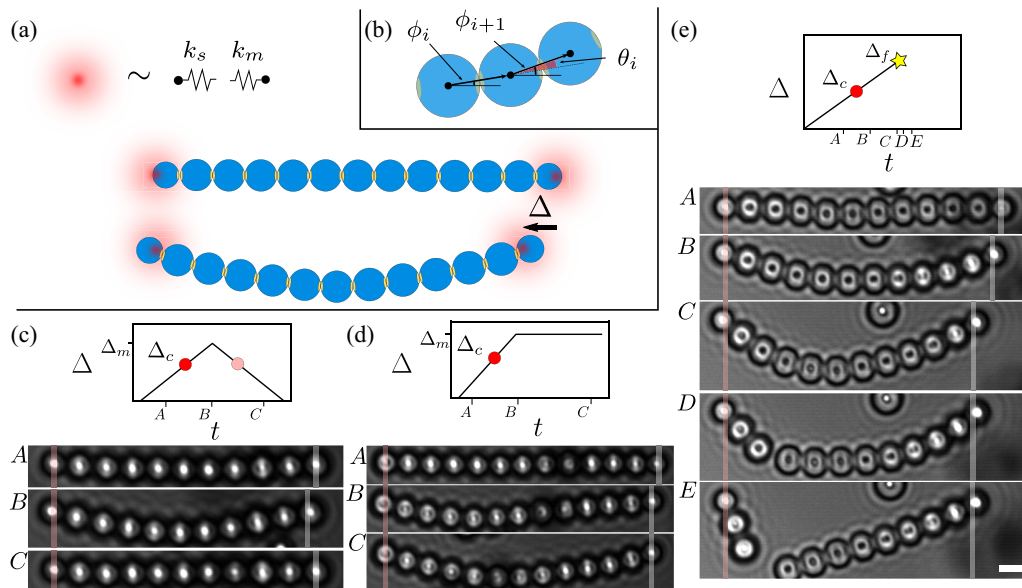


FIG. 1. Micromechanical tests of dipatch particle chains with optical tweezers. (a) Sketch of a dipatch particle chain in two harmonic optical traps. (b) Sketch illustrating the bending angle definition. (c) Cyclic buckling test protocol and example snapshots at times (A) before buckling, (B) at maximum compression, and (C) after reversible straightening. (d) Relaxation test protocol and snapshots at times (A) before buckling, (B) when trap movement is stopped reaching Δ_m , and (C) after waiting 100 s at Δ_m . (e) Fracture test protocol, snapshots in (A) initial and (B) buckled state, (C) at 1 s before, (D) at 1 s after, and (E) at 7 s after break-up. Red (white) transparent lines in the snapshots correspond to the x position of the fixed (mobile) trap. Scale bar is $3 \mu\text{m}$.

results provide insight into the mechanics of assembled colloidal structures that is essential to design functional colloidal architectures.

II. METHODS

A. Chain formation and micromechanical compression test protocols

Monodispersed dipatch particles of diameter $d = 3.1(1)\mu\text{m}$ are synthesized from polystyrene (bulk material) and fluorescently labeled 3-(trimethoxysilyl)propyl methacrylate (TPM, surface patches) using a recently published colloidal fusion method [22,24]; they have small hemispherical patches of diameter $d_p = 380 \text{ nm}$, with patch arc-angle $\theta_p = 2 \sin^{-1}(d_p/d) = 14^\circ(\pm 2)$, as measured by atomic force microscopy. Patch characterization details can be found in Ref. [23]. In addition, a minor fraction of monopatch particles of diameter $d = 2.7(1)\mu\text{m}$ are also present in the sample. The particles are suspended in a binary mixture of water and lutidine with lutidine volume fraction $c_L = 0.25$, in which they sediment to form a quasi-two-dimensional layer. We also added 0.375 mM magnesium sulfate to screen the particle charges and increase the lutidine absorption contrast of the patches. This binary mixture is chosen to obtain optimal critical Casimir conditions with a largest temperature window for patch-to-patch attraction. The dipatch particles self-assemble into chains in a capillary coupled to a double optical tweezer setup, when heating the suspension to $\Delta T = 0.1^\circ\text{C}$ below the solvent critical temperature $T_c = 33.75^\circ\text{C}$. The sample capillary is sandwiched between the water immersion objective and condenser lenses. Custom-made objective and condenser-lens

heaters are used to maintain the sample temperature with a stability of 0.05°C . We wait for more than 3 h for the system to equilibrate such that sufficiently long chains assemble. We then select chains consisting of $N = 6\text{--}13$ particles that consist of a sufficient number of monomers and are still observed at sufficient frequency, and we pin their ends using optical tweezers. Preferably, we use dipatch chains that have monopatch particles capping their ends. These capped chains have the advantage that no other chain can attach during the experiment.

We use a (static) trap, which always remains in a fixed position, and a piezoelectrically controlled mobile trap, which is moved at a speed of around $v_{\text{trap}} \approx 0.01 \mu\text{m/s}$, exerting an increasing compressive force on the chain. A schematic of the setup is shown in Fig. 1(a). Here, the trap displacement Δ is defined as the distance of the mobile trap from its initial position, and the trap velocity $v_{\text{trap}} = \frac{d\Delta}{dt}$. The optical tweezer setup has been described elsewhere [25]. The two laser beams with wavelength 1064 nm and a low intensity of $\sim 5 \text{ mW}$ each were focused in narrow spots using a water immersion high-NA imaging objective. The low intensity ensured that no solvent phase separation occurred due to local heating at the traps; we estimate the local heating to be maximally 0.05 K from measurements at higher intensity where phase separation occurred in the laser focus. Furthermore, the trapped particles retained in-plane rotational freedom; although optical trapping confines the patches to the horizontal plane, the patches still rotate freely around the vertical laser beam axis, as shown in the Supplemental Material [26–30].

To a good approximation, the static and mobile traps form harmonic traps, with spring constants k_s and k_m , respectively. The calibration of the spring constants is described in the Supplemental Material [26]. We can thus infer the force on

the chain from the calibrated spring constant k_s and the bead displacement out of the static trap center with bright-field microscopy, using $F = k_s(x_s - x_1)$, where x_s and x_1 are the x -coordinates of the trap center and the trapped particle, respectively. Here, the coordinate system has been chosen to be aligned with the chain. The linear compression u is defined by $u = L_0 - L$ with the equilibrium total (contour) length $L_0 = \sum d_i$, with d_i the distance between two bonded particles when no stress is applied, and the actual end-to-end distance L , defined by $L = x_N - x_1$.

To interrogate the mechanical response of the colloidal chain, we have performed three different micromechanical tests: (i) A cyclic buckling test, (ii) a stress-relaxation test, and (iii) a fracture test. Each test starts by catching the capping beads of an assembly in a relaxed configuration and is designed to probe different mechanical properties of the chains, respectively: elastic buckling, viscoelastic/plastic deformation, and ultimately break-up. During (i), the mobile trap is moved with constant speed v_{trap} toward the fixed trap until a maximum trap displacement $\Delta = \Delta_m \sim 1 \mu\text{m}$, significantly above the buckling threshold, and then returned to its initial position. During (ii), the mobile trap is moved similarly to a maximum $\Delta = \Delta_m$, but then kept fixed for a certain amount of time, during which the system can relax the stress through plastic deformation, as measured by a reduction of the force exerted on the static particle. During (iii), the trap is moved continuously until a point of failure is reached and the chain breaks.

During these experiments, the chains are imaged using bright-field microscopy at a frame rate of 20 fps with a pixel size of 87.7 nm. The centers of each particle within the chain are localized in the imaging plane with a subpixel accuracy of $\epsilon = 10 \text{ nm}$ using particle tracking software [31]. The resulting particle positions $r_i = (x_i, y_i)$ are used to compute the nearest-neighbor distances $d_i = ||r_{i+1} - r_i||$ and bond tangent angles $\phi_i = \arctan(y_{i+1} - y_i)/(x_{i+1} - x_i)$. We define the local bending angle $\theta_i = \phi_{i+1} - \phi_i$ at particle i from the two neighboring bond angles, ϕ_i and ϕ_{i+1} , as illustrated in Fig. 1(b). To study the (vibrational) modes under the increasing compression and compare with continuum theories of elastic filaments, we perform a Fourier transform according to

$$M_i = \frac{2}{N-1} \sum_{j=1}^{N-2} y_j \sin\left(\frac{\pi}{N-1} j i\right), \quad i = 1, \dots, N-2. \quad (1)$$

Here, y_i is the deflection perpendicular to the line connecting the two trapped particles, and i runs from 1 to $N-2$ as the first and last particles are fixed in the y -direction by construction.

III. RESULTS AND DISCUSSION

An overview of the micromechanical tests together with representative snapshots of the colloidal chain are shown in Fig. 1. Upon compression, we observe that above a critical compression Δ_c the initially straight chain buckles. This buckling is reversible as shown in the cyclic compression test in Fig. 1(c): upon unloading, the chain reversibly straightens out, suggesting an elastic response at the moderate strain probed here $u/L_0 \lesssim 0.01$. However, when the trap is kept

fixed at a larger compression after buckling, reaching strains $u/L_0 \gtrsim 0.01$, viscoelastic effects come into play [Fig. 1(d)]. The deflection keeps increasing at fixed end-to-end distance, indicating creep of the chain. This creep response is accompanied by stress relaxation, as can be seen by the trapped particles relaxing back to the trap center. Finally, if we keep increasing the compression beyond the break-up displacement Δ_f , the chain breaks at a single connection point and two bonded patches separate, as shown in Fig. 1(e). After break-up, the two remaining ends quickly release their elastic energy by straightening out, further showing the reversibility of the remaining two chain segments.

A. Elastic Euler buckling

To obtain insight into the buckling transition, we determine the force quantitatively from the displacement of the particle out of the static trap. A typical force-trap displacement curve during cyclic loading is shown in Fig. 2(b). Initially, the force increases linearly with trap displacement; the initial slope fits to $k_\Delta = 0.25 \text{ pN}/\mu\text{m}$, which agrees with the effective spring constant of the two traps placed in series, $k_{\text{eff}} = 1/(1/k_s + 1/k_m) = 0.24 \pm 0.03 \text{ pN}/\mu\text{m}$, where we have used the calibrated spring constants $k_s = 0.58 \pm 0.02 \text{ pN}/\mu\text{m}$ and $k_m = 0.42 \pm 0.05 \text{ pN}/\mu\text{m}$. Thus, in the prebuckling regime, only the trap springs are compliant, and the chain is incompressible within measurement accuracy. At a critical trap displacement Δ_c , the chain buckles, and the force saturates at a plateau F_c . Upon unloading, a mirrored response occurs, and the buckling vanishes at a critical displacement of Δ'_c . Pinpointing the critical displacements Δ_c and Δ'_c by interpolation, we find that they are very similar; their difference $\Delta_c - \Delta'_c = (0.1 \pm 0.1) \mu\text{m}$ is of the order of the experimental uncertainty. This reversible behavior indicates an elastic response on these timescales. This is confirmed when we compute the dissipated energy by integration of the fitted force curves, which yields $\oint F d\Delta \sim 2k_B T$, of the order of the thermal energy.

We determine the actual physical compression of the chain using the images to locate the chain end points. The corresponding force versus real strain u/L_0 shows a steep, almost vertical increase of the force [Fig. 2(c)], confirming the near-incompressible character of the chain. The sharp transition to a constant force at the critical force F_c is strongly reminiscent of the elastic response of classical Euler buckling [32–34]. The latter states that a freely hinged elastic rod of bending rigidity B buckles out of its straight configuration into the lowest-order mode at a load $F_c^e = \pi^2 B/L_0^2$. The mode strain amplitude itself is described by $M^e/L_0 = 2/\pi \sqrt{u/L_0}$. Indeed, after buckling, the colloidal chain assumes a characteristic first-mode deflection as shown in Fig. 1(c), and confirmed by plotting the extracted first-mode amplitude M_1 as a function of strain in Fig. 2(d). The amplitude closely follows the Euler prediction for M^e , as shown by the dashed curve through the data points. This agreement with the Euler model further indicates that for moderate strains, the response of the chain is predominantly elastic, and viscous contributions are minimal. Compared to simple linear aggregates of isotropic particles that also exhibit buckling behavior [35], the behavior observed here is in even much better agreement with continuum theory.

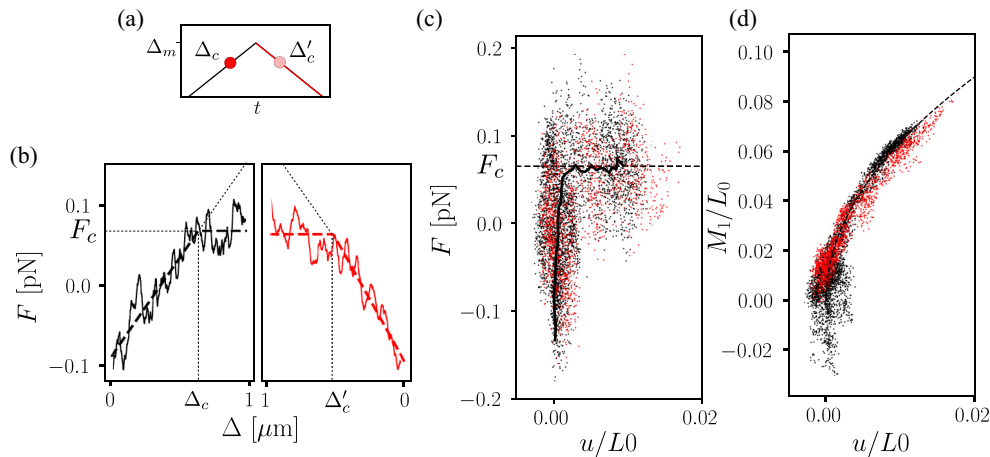


FIG. 2. Reversible elastic Euler buckling. (a) Schematic of the applied displacement as a function of time. (b) Force vs trap displacement of the loading (black) and unloading cycle (red); data are smoothed by a running average over 100 frames. Dashed lines are fits to an initial linear force increase followed by a plateau. The force starts out negative as chains are kept in a stretched state before starting the experiment. (c) Force vs strain; dots are individual data points, the black line is a running mean performed by rotating the axes by 45° . The dashed line is the best fit to the data for $u/L_0 > 0.005$, defining F_c . (d) Normalized first-mode amplitude vs strain. The dashed line represents an ideal first-mode deflection described by $M_1/L_0 = 2/\pi \sqrt{u/L_0}$. All data correspond to a single typical experiment of an $N = 11$ chain with $\Delta_m = 1 \mu\text{m}$ at $v_{\text{trap}} = 0.01 \mu\text{m/s}$; corresponding images are shown in Fig. 1(c).

This is likely due to the more perfect straightness of the chain afforded by the dipatch particle geometry.

To confirm this behavior and obtain more insight into the impact of chain length on bending and buckling characteristics, we repeated the experiment for chains of different lengths, and we determined accurate values of F_c for each experiment by averaging F in the plateau regime for data points with $u/L_0 > 0.005$ and $u/L_0 < 0.01$. The extracted values of F_c as a function of chain lengths show a characteristic decrease in Fig. 3(a). By fitting with the Euler dependence L_0^{-2} (black line), we obtain the bending rigidity $B = 10 \text{ pN } \mu\text{m}^2$, corresponding to a persistence length $L_p = B/k_B T = 2400 \mu\text{m}$. This is remarkably close to the short-time bending rigidity $L_p^{\text{fast}} = 2420 \mu\text{m}$ obtained from quiescent, free chains by analysis of their thermal vibrations [23]. Using the Euler equation, we can also determine B and L_p separately for each experiment from the measured F_c and plot it as a function of L_0 ; see Fig. 3(b). Despite the scattering of the data, likely caused by the polydispersity in the patch size, temperature fluctuations,

and experimental error, there is a notable trend towards lower rigidities for smaller chains. We associate this trend with the larger bond angles for shorter chains and enhanced plastic effects that reduce the effective rigidity. Another reason could be the dynamic excitation of the first mode, which for longer chains needs more time (growing with L_0^4 [23]). As the speed of the trap movement is always similar, this could lead to excitation of higher-order modes increasing the stress, as observed for macroscopic elastic filaments [36,37].

We conclude that for moderate strains of up to around $u/L_0 \sim 1\%$, the chains show elastic Euler buckling, reversible upon unloading and in line with the rigidity found from short-time fluctuations. However, a trend of decreasing bending rigidity for shorter chains points to possible plastic effects or excitation of dynamic higher-order modes.

B. Creeping and stress relaxation

To obtain further insight into these viscoelastic effects, we investigate the creep response of the chain held at constant compression after buckling. The corresponding trap displacement, force, first-mode amplitude, and compression are shown over the full cycle of initial loading and subsequent creep in Fig. 4(a). Shortly after buckling (red dot), the trap movement is stopped (red star). Interestingly, despite the constant trap positions [plateau in Fig. 4(a), top], the first-mode amplitude continues to rise [Fig. 4(a), third panel], while the compressive force decreases and relaxes towards zero. This force relaxation cannot be attributed to equilibration of the trap, as there was no asymmetry in the force measurement obtained from static versus mobile traps (data not shown). To complete the compression-relaxation cycle, when the chain has fully relaxed, we quickly unload. Again, a delayed response is observed with u and M_1 decaying after trap movement has stopped.

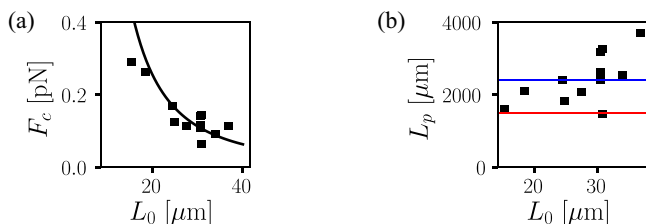


FIG. 3. Critical buckling force and persistence length. (a) Buckling force vs chain rest length of 11 experiments. The solid line is a fit to the Euler criterion $F_c = \pi^2 B/L_0^2$. (b) Resulting persistence length, calculated by inversion of Euler's criterion for each measurement. The blue (red) line corresponds to $L_p^{\text{fast}} = 2420 \mu\text{m}$ ($L_p^{\text{slow}} = 1500 \mu\text{m}$), previously obtained from analysis of thermally activated relaxation [23].

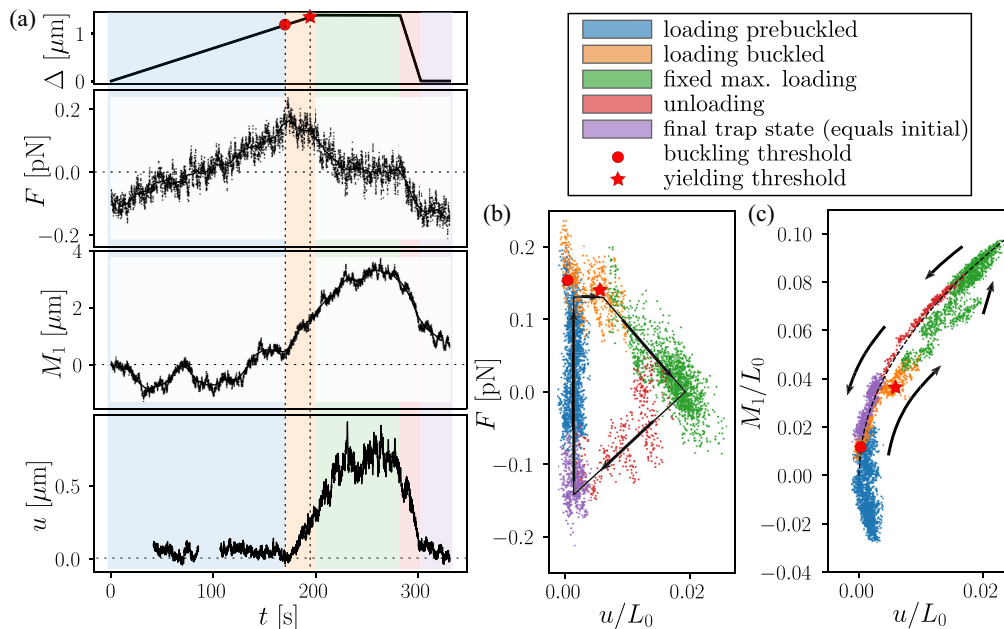


FIG. 4. Creep tests revealing viscoelastic dissipation. (a) Time traces of trap displacement, force, first-mode amplitude, and strain of a chain undergoing a stress relaxation protocol followed by a quick unloading. The red dot indicates buckling, and the red star indicates yielding. (b), (c) Force (b) and first-mode amplitude (c) vs strain. Arrows indicate the time direction. The color coding of data points corresponds to the background color of (a), which indicates the phase of the experiment; see the legend. The red star and dot consistently indicate the buckling and yielding points. The dashed line in (c) corresponds to an ideal first-mode deflection. Data correspond to a representative experiment of an $N = 13$ particle chain with $\Delta_m = 1.3 \mu\text{m}$ at $v_{\text{trap}} = 0.0075 \mu\text{m/s}$. Corresponding images are shown in Fig. 1(d).

Looking at the force as a function of compression in Fig. 4(b), we notice a pronounced hysteresis: after the initial Euler-like response (sharp rise of F followed by a plateau until the red star), the compression keeps growing at a declining force, indicating significant slow relaxation until the force vanishes. Upon subsequent unloading and restoring the initial trap positions, the compression decreases and finally vanishes and the cycle is complete. The extended area inside the cycle indicates significant energy dissipation. By rough interpolation of the data, we can integrate and find $\Delta E_u^\circ = \oint F du = 21 k_B T$, significantly higher than thermal energy. Concomitantly, the first-mode amplitude as a function of compression [Fig. 4(c)] shows some interesting deviation from the Euler prediction after buckling (red star): the amplitude deviates from a pure first mode deformation (indicated by the dotted line). This deviation to a lower amplitude M_1 indicates that higher bending modes are excited, different from the pure Euler buckling observed before. A visual signature of this can be seen in the image of the chain in Fig. 1(d)-B, which shows asymmetric bending.

To understand this dissipative process in more detail, we focus on the relaxation period when the trap movement has stopped [$t > t_2 = 200$ s in Fig. 5(a)]. The evolution of the force, first-mode amplitude, and compression are shown in Figs. 5(b)–5(d). The evolution of both force and compression are well described by monoexponential relaxations,

$$F = F_i e^{-\Delta t/\tau_F}, \quad u = u_f - u_{\text{creep}} e^{-\Delta t/\tau_u}, \quad (2)$$

where $\Delta t = t - t_2$, $F_i = 0.13$ pN is the initial force, u_f is the final displacement, and $u_{\text{creep}} = 0.46 \mu\text{m}$ is the total creep displacement. From the fits, we obtain relaxation times of

$\tau_F = 13 \pm 1$ s and $\tau_u = 14 \pm 1$ s, which agree with each other within error bars. We also fit a monoexponential relaxation to M_1 and find $\tau_{M_1} = 22 \pm 1$ s. For a pure first-mode deformation, one expects $M_1 \propto \sqrt{u}$, and hence $\tau_{M_1} = 2\tau_u = 28$ s [33]. The slightly faster first-mode relaxation observed here is likely caused by additional relaxation of higher modes into the first-mode, speeding up first-mode growth.

These results can be interpreted within a minimal mechanical model, outlined in Fig. 5(e). Before buckling, the system response is described by two springs in series, namely the effective trap spring with constant $k_{\text{trap}} = (1/k_s + 1/k_m)^{-1}$, and the straight chain with k_{chain} [Fig. 5(e), top panel]. Since $k_{\text{chain}} \gg k_{\text{trap}}$, mostly the traps compress, while the chain is hardly compressible. After buckling ($t > t_1$, and $\Delta > \Delta_c$), the chain becomes compliant, resisting with a constant force F_c . At even higher strain (time t_2 , and $\Delta = \Delta_\eta$), the chain yields, being described by a dashpot with effective viscosity η' . The mechanical response of the system can be summarized using the following constitutive equations [38]:

$$\begin{aligned} F &= k_{\text{trap}}(\Delta - \Delta_0), \quad u = 0 \quad \text{for } \Delta < \Delta_c, \\ F &= F_c, \quad u = \Delta - \Delta_c \quad \text{for } \Delta_c < \Delta < \Delta_\eta, \\ \dot{\Delta} &= \frac{\dot{F}}{k_{\text{trap}}} + \frac{F}{\gamma'}, \quad \dot{u} = \frac{F}{\gamma'} \quad \text{for } \Delta_\eta < \Delta, \end{aligned} \quad (3)$$

where Δ_0 is the equilibrium trap distance, and γ' is a drag coefficient associated with an effective viscosity $\gamma' = \eta' A/L_0$ via an area A . We assume that there is no creep before the trap is fixed, hence $\dot{\Delta} = 0$ in the creep regime and Δ_η coincides with the maximum trap displacement Δ_m . Then line 3 of

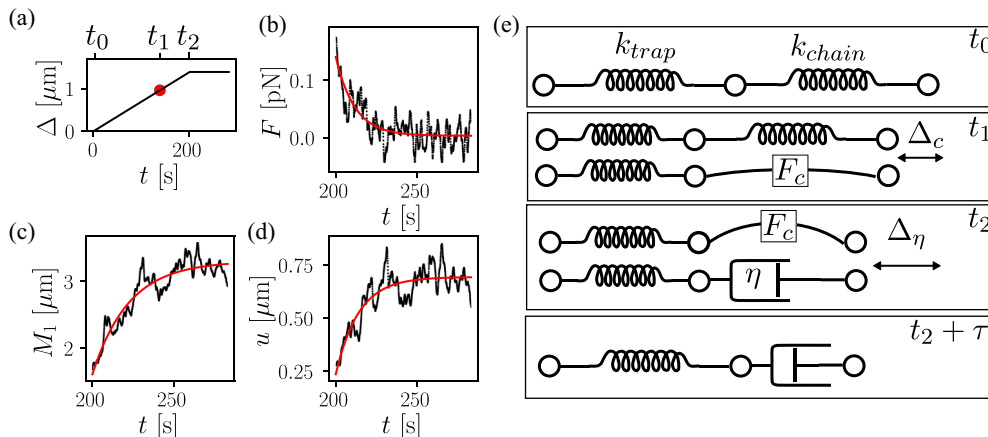


FIG. 5. Stress relaxation test and model. (a) Displacement protocol used for the stress-relaxation experiment. (b)–(d) Relaxation of the force, first-mode amplitude, and compression of the chain as a function of time starting at t_2 . Red lines are monoexponential fits. (e) Macroscopic mechanical model for the combined system of harmonic trap and viscoelastic chain. As a function of trap displacement, the system shows a different mechanical response. Before buckling, the chain behaves elastically, and there are two springs in series (top panel). When $\Delta > \Delta_c$, the chain buckles and the system transitions to a spring and a compliant chain resisting with constant force F_c (second panel, parallel chains refer to the transition). When $\Delta > \Delta_\eta$, the chain becomes viscoelastic, and the system transitions to a spring and a dashpot with effective viscosity η' . The fourth panel shows the situation after a time τ in which relaxation has occurred.

Eq. (3) is simply solved by

$$F = F_c e^{-k_{\text{trap}} t / \gamma'}, \quad u = -\frac{F_c}{k_{\text{trap}}} e^{-k_{\text{trap}} t / \gamma'} + u(t = t_2). \quad (4)$$

The model thus correctly predicts monoexponential decays with equal decay times for force and strain, as seen in the fits of Eq. (2). Using the fitted values, we obtain $F_c = F_i$, $k_{\text{trap}} = F_i / u_{\text{creep}} = 0.3 \text{ pN}/\mu\text{m}$, and $\gamma' = 4 \text{ Pa s } \mu\text{m}$. The spring constant and F_c agree well with the values obtained for the loading and buckling regime. Moreover, any potential overestimation of k_{trap} with respect to the expected value $(1/k_s + 1/k_m)^{-1} = 0.26 \text{ pN}/\mu\text{m}$ is likely due to the assumption that there is no creep before reaching the maximum trap displacement $\Delta_\eta = \Delta_m$. Yielding probably occurred slightly earlier at the point where higher modes got excited. We also note that the extracted drag coefficient γ' can be used to estimate the dissipated energy from the loading and unloading rates in Fig. 4(a) (bottom). Integrating $F = \gamma' \dot{u}$ over the loading and unloading cycle using slopes between $\dot{u} = 0.013$ and $0.008 \text{ } \mu\text{m}/\text{s}$ for the loading rate and $\dot{u} = 0.026 \text{ } \mu\text{m}/\text{s}$ for the unloading rate, we obtain dissipated energies between 19 and $23 k_B T$, in good agreement with the value of $21 k_B T$ determined from integration over the cycle. For such a minimal model, the agreement is striking.

The question now is, what is the origin of the drag coefficient γ' ? From elastic relaxation of free chains, we extracted a fluid drag coefficient $\gamma_{M_1} = 50 \text{ m Pa s } \mu\text{m}$ (data not shown), two orders of magnitude lower than γ' . We thus conclude that the source of the drag cannot be the outside fluid, but most likely comes from internal patch-patch friction of the chain. This is in agreement with our conclusion from quiescent chains subjected to thermal excitation [23]. These measurements showed that on timescales $t > 10 \text{ s}$, dissipative effects take place, associated with internal friction with an effective viscosity of $\sim 1 \text{ Pa s}$.

We can estimate that the effective viscosity η' that is associated with the drag coefficient γ' is $\eta' = \gamma' L_0 / A = 14 \text{ Pa s}$,

where the area $A = d^2$. The origin of this dissipation is the occurrence of slow conformational changes, likely due to contact slippage [23]. The real-space snapshots suggest that indeed the higher-order modes localize bending on a single bond, indicating bond slip. Initially, this slip is localized on a particular bond, but with increasing strain the localization diminishes, and more bonds get involved in the bending, until finally a pure first-mode buckling is recovered. This behavior is reminiscent of the relaxation that occurs in actin bundles, which also show a slow viscoelastic buckling relaxation when compressed with optical tweezers [7]. In the case described there, though, the yielding is due to internal restructuring of the polymers. In addition, quiescent experiments of fluctuating microtubules also show significant viscoelastic behavior attributed to internal friction [6]. It is surprising that a simple chain assembled from divalent particles shows similar rheological behavior, suggesting that these relaxation phenomena are general.

C. From bending to break-up

At even larger strains, the dipatch particle chains show a transition from bending to break-up, as depicted in the microscope images in Figs. 6(a) and 6(b). The large applied strain, reaching about $u/L_0 \sim 10\%$, causes a strong chain bending. At the break-up strain u_b/L_0 , the chain breaks at a single bond, after which the average force reduces to zero. The average bending angle (black) and the bending angle associated with the bond that breaks (red) are shown in Fig. 6(c). The average bending angle increases until the break-up point, reaching a maximum $\langle \theta \rangle_b$. The bond that breaks has a higher than average bend angle at the moment of break-up. Right after break-up, the average bend angle of the two broken chain parts straightens out quickly and relaxes to zero [Fig. 6(d)]. The timescale of straightening is of the order of only a few seconds, indicating fast elastic relaxation, limited by solvent friction.

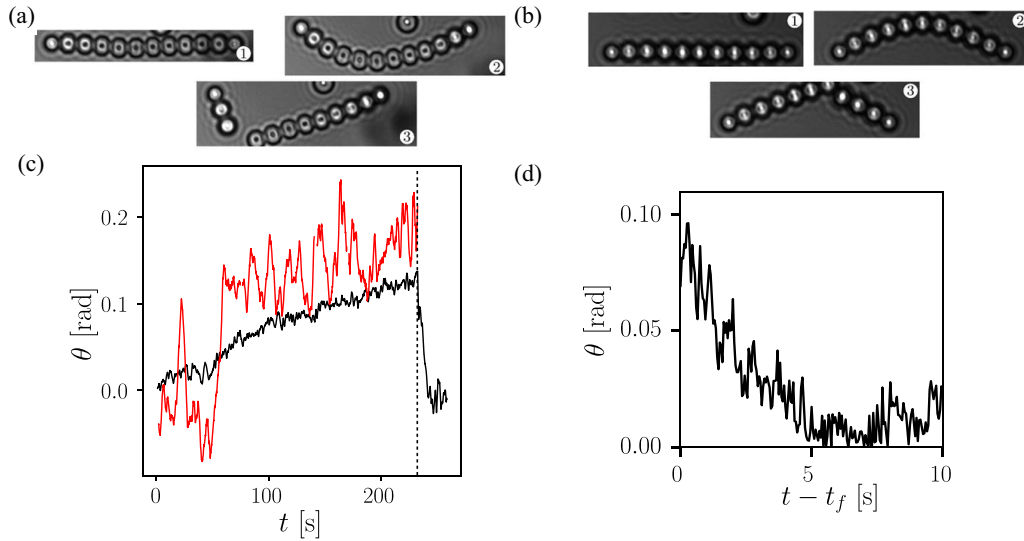


FIG. 6. Break-up at high applied strain. (a), (b) Bright-field microscope images of the dipatch particle chains under compression, before and after break-up. The chain does not always break in the middle where the highest curvature is located. This can be explained by thermal noise or polydispersity in the patch size, leading to local variations in stiffness along the chain. (a) Chain with $N = 12$, compressed at $v_{\text{trap}} = 0.015 \mu\text{m/s}$. (b) Chain with $N = 11$ particles compressed at $v_{\text{trap}} = 0.02 \mu\text{m/s}$. (c) Bending angles of bonded particles vs time showing continuous increase until break-up, and rapid straightening thereafter (data correspond to the $N = 12$ chain). The black line is the average of all bending angles $\langle \theta \rangle$, the red line is the mean of the two bending angle next to the broken bond. The vertical dashed line marks the time t_b at which the chains break. (d) Relaxation of the average bending angle as a function of elapsed time after break-up. The timescale is of the order of a few seconds, characteristic for elasticlike relaxation damped by the solvent.

To elucidate the breaking process in more detail, we performed six breaking experiments and plot their break-up strains as a function of chain length in Fig. 7(a). A clear systematic increase is observed. This is to be expected as chains with more particles show less local bending per bond for the same strain. In fact, the average bending angle $\langle \theta \rangle_b$ at break-up appears almost insensitive to the chain length, with an average $\langle \theta \rangle_b = 0.11(1)$ rad; see Fig. 7(b). This suggests that $\langle \theta \rangle_b$ is a critical bending angle that we can use as a predictive criterium for break-up. We also plot an alternative bending angle, $\langle \theta_{M_1} \rangle_b$, corresponding to the average bending angle in the case of a pure first mode deformation, defined by $\langle \theta_{M_1} \rangle_b = 2\pi dM_{1,b}/L_0^2$ (blue data points). These two quantities overlap well, further showing that deformation is close to that of a pure first mode; hence, $\langle \theta_{M_1} \rangle_b$ forms an equivalent critical bending criterium. We can use this criterium together with the relation $M_1/L_0 = 2\sqrt{u/L_0}/\pi$ to obtain a

prediction for the break-up strain $u_b/L_0 = (L_0/d)^2 \langle \theta_{M_1} \rangle_b^2 / 16$, which is indicated by the blue line in Fig. 7(a). Given that there are no fitting parameters in this prediction for the break-up strain, the agreement with experiment is remarkable.

How does this critical bending angle relate to the patch size? The patch has a diameter of approximately $d_p = 0.38(5) \mu\text{m}$, which translates to an arc angle $2 \sin^{-1}(d_p/d) = 0.14(2)^\circ = 0.24(3)$ rad. Here, the uncertainty is an estimation of the particle patch area polydispersity. As the critical Casimir interaction is short-ranged, and the bonds weaken increasingly as the patches become inclined [39], we expect that the chain breaks when one bond angle reaches the patch arc angle, as illustrated in Fig. 7(d). The critical bending criterion thus translates to a maximum bending angle $\max(\theta_{M_1})_b = \pi \langle \theta_{M_1} \rangle_b / 2 = 0.17(1)$ rad. This is indeed close to the patch arc angle, yet it is slightly smaller, meaning chains break

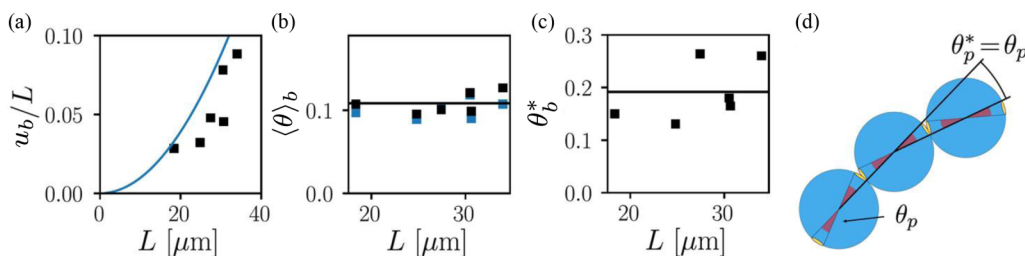


FIG. 7. Critical bending angle of break-up. (a) Maximum strain reached right before break-up as a function of chain length. The blue line is a prediction based on a maximum bending criterium; see the text. (b) Mean bending angle right before break-up vs chain length; the black line is the average. (c) Maximum bending angle of the bond that snaps; the black line is the average. (d) Schematic illustrating that the expected maximum bond bending angle θ_p^* equals the patch arc angle θ_p .

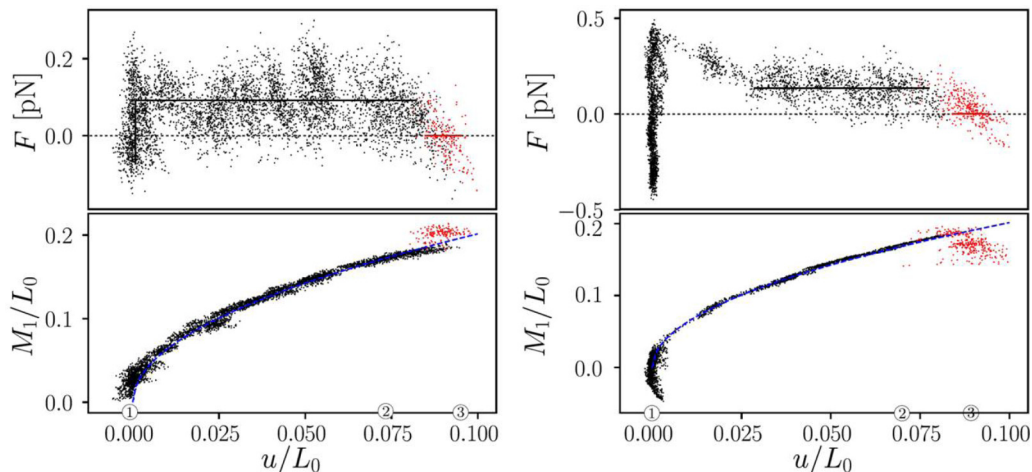


FIG. 8. Large-strain Euler buckling accompanied by stick-slip relaxation. Force (top) and first-mode deflection (bottom) vs strain of the two representative breaking tests in Fig. 6. Red dots are post break-up data points. Numbers correspond to those in Fig. 6. The data suggest some stick-slip-like relaxation at larger strain before break-up.

slightly earlier than this limit. The difference can be explained by patch size polydispersity and thermal fluctuations that can spontaneously increase the local bending, as visible in the red curve of Fig. 6(c). In fact, the actual measured bending angle θ_b^* of the bond that snaps is typically higher than 0.17 rad, as shown in Fig. 7(c). Averaging over all the measurements yields $\bar{\theta}_b^* = 0.20(5)$ rad, consistent within accuracy with the patch arc angle. From this correspondence we conclude that the breaking transition arises from the limited patch size, which explains the striking difference with the response of isotropic particle chains [35].

Like before, we observe force and deflection curves that are very reminiscent of the elastic Euler buckling behavior, now up to the break-up point (Fig. 8). This apparent elastic response is supported by the characteristic elastic relaxation back to the linear chain configuration after break-up [Fig. 6(d)]. Given that these large strains exceed the viscoelastic yield strain, this is surprising. Indeed, upon close inspection of Fig. 8 (top left), the data suggest that some stick-slip behavior occurs: in the plateau regime instead of a constant force, a sequence of stress buildups and decays seems to occur, suggesting that even before break-up, some nonelastic relaxation occurs.

This nonelastic relaxation is very limited, however, as the probing is fast: the chain does not have time to fully relax at the applied loading rate ($v_{\text{trap}} \sim 0.02 \mu\text{m/s}$, more than twice as fast as in the relaxation experiment). This applied loading rate is close to the plastic relaxation rate, which we estimate from the postyielding creep rate as $\dot{u} = \frac{F}{\gamma'} \sim 0.025 \mu\text{m/s}$. Here, we have used the previously obtained value for the internal drag coefficient $\gamma' = 4 \text{ Pa s } \mu\text{m}$ and the force $F \sim 0.1 \text{ pN}$. Hence, while the chains do not have time to fully relax, they exhibit some minor viscous relaxation in the otherwise elastic process. Unfortunately, the experimental noise caused

by thermal fluctuations does not allow us to be more quantitative on this point.

IV. CONCLUSIONS

We have shown that chains of dipatch colloidal particles buckle elastically, closely following the macroscopic Euler buckling behavior when the strain is kept below the yield strain. The elastic Euler buckling recovers the $F_c \propto L^{-2}$ scaling of buckling load with filament length, and it yields a persistence length that agrees well with fluctuation measurements on quiescent chains [23]. For larger strains and on longer timescales, viscoelastic effects lead to stress-relaxation. This viscoelastic relaxation is attributed to internal friction due to bond slippage. We used a simple linear viscoelastic model that provided a good fit to the experimental stress-relaxation data. Finally, we showed that upon further increase of the strain, at a critical maximum bending angle, the chains break. This maximum bending angle can be rationalized based on the size of the patch and thermal noise. Hence, the finite patch size is essential not only for determining the structures formed through self-assembly, but also for their resulting mechanical stability.

These results highlight the rich nonlinear, viscoelastic, and break-up mechanics present in assembled patchy particle structures, the essential features of which we can model and predict accurately. The elastic loading, viscoelastic relaxation with apparent stick-slip dynamics, and final failure of the chains are reminiscent of the complex nonlinear mechanics of biological materials. These results suggest that patchy particle assembly is a promising route to achieve “colloidal architectures,” micron-scale structured materials with designer mechanical properties, further extending the use of patchy particle systems.

[1] K. D. Costa, W. J. Hucker, and F. C.-P. Yin, Buckling of actin stress fibers: A new wrinkle in the cytoskeletal tapestry, *Cell Motil. Cytoskeleton* **52**, 266 (2002).

[2] M. Kikumoto, M. Kurachi, V. Tosa, and H. Tashiro, Flexural rigidity of individual microtubules measured by a buckling force with optical traps, *Biophys. J.* **90**, 1687 (2006).

- [3] V. Kantsler and R. E. Goldstein, Fluctuations, Dynamics, and the Stretch-Coil Transition of Single Actin Filaments in Extensional Flows, *Phys. Rev. Lett.* **108**, 038103 (2012).
- [4] O. V. Kim, R. I. Litvinov, J. W. Weisel, and M. S. Alber, Structural basis for the nonlinear mechanics of fibrin networks under compression, *Biomaterials* **35**, 6739 (2014).
- [5] S. Kumar, I. Z. Maxwell, A. Heisterkamp, T. R. Polte, T. P. Lele, M. Salanga, E. Mazur, and D. E. Ingber, Viscoelastic retraction of single living stress fibers and its impact on cell shape, cytoskeletal organization, and extracellular matrix mechanics, *Biophys. J.* **90**, 3762 (2006).
- [6] C. P. Brangwynne, G. H. Koenderink, E. Barry, Z. Dogic, F. C. MacKintosh, and D. A. Weitz, Bending dynamics of fluctuating biopolymers probed by automated high-resolution filament tracking, *Biophys. J.* **93**, 346 (2007).
- [7] F. R uckerl, M. Lenz, T. Betz, J. Manzi, J.-L. Martiel, M. Safouane, R. Paterski-Boujemaa, L. Blanchoin, and C. Sykes, Adaptive response of actin bundles under mechanical stress, *Biophys. J.* **113**, 1072 (2017).
- [8] J. Block, H. Witt, A. Candelli, J. C. Danes, E. J. G. Peterman, G. J. L. Wuite, A. Janshoff, and S. K oster, Viscoelastic properties of vimentin originate from nonequilibrium conformational changes, *Sci. Adv.* **4**, eaat1161 (2018).
- [9] D. J. Odde, L. Ma, A. H. Briggs, A. DeMarco, and M. W. Kirschner, Microtubule bending and breaking in living fibroblast cells, *J. Cell Sci.* **112**, 3283 (1999).
- [10] T. Sanchez, D. T. N. Chen, S. J. DeCamp, M. Heymann, and Z. Dogic, Spontaneous motion in hierarchically assembled active matter, *Nature (London)* **491**, 431 (2012).
- [11] A. D. Dinsmore, V. Prasad, I. Y. Wong, and D. A. Weitz, Microscopic Structure and Elasticity of Weakly Aggregated Colloidal Gels, *Phys. Rev. Lett.* **96**, 185502 (2006).
- [12] Q. Chen, J. K. Whitmer, S. Jiang, S. C. Bae, E. Luijten, and S. Granick, Supracolloidal reaction kinetics of janus spheres, *Science* **331**, 199 (2011).
- [13] A. McMullen, M. Holmes-Cerfon, F. Sciortino, A. Y. Grosberg, and J. Brujic, Freely Jointed Polymers Made of Droplets, *Phys. Rev. Lett.* **121**, 138002 (2018).
- [14] E. M. Furst and A. P. Gast, Micromechanics of Dipolar Chains using Optical Tweezers, *Phys. Rev. Lett.* **82**, 4130 (1999).
- [15] E. M. Furst and J. P. Pantina, Yielding in colloidal gels due to nonlinear microstructure bending mechanics, *Phys. Rev. E* **75**, 050402(R) (2007).
- [16] V. N. Manoharan, Colloidal matter: Packing, geometry, and entropy, *Science* **349**, 1253751 (2015).
- [17] Z. Zhang and S. C. Glotzer, Self-assembly of patchy particles, *Nano Lett.* **4**, 1407 (2004).
- [18]  . Duguet, C. Hubert, C. Chomette, A. Perro, and S. Ravaine, Patchy colloidal particles for programmed self-assembly, *C. R. Chim.* **19**, 173 (2016).
- [19] M. Kurachi, M. Hoshi, and H. Tashiro, Buckling of a single microtubule by optical trapping forces: Direct measurement of microtubule rigidity, *Cell Motil. Cytoskeleton* **30**, 221 (1995).
- [20] J. van Mameren, K. C. Vermeulen, F. Gittes, and C. F. Schmidt, Leveraging single protein polymers to measure flexural rigidity, *J. Phys. Chem. B* **113**, 3837 (2009).
- [21] C. P. Broedersz and F. C. MacKintosh, Modeling semiflexible polymer networks, *Rev. Mod. Phys.* **86**, 995 (2014).
- [22] S. Stuij, J. Rouwhorst, H. J. Jonas, N. Ruffino, Z. Gong, S. Sacanna, P. G. Bolhuis, and P. Schall, Revealing Polymerization Kinetics with Colloidal Dipatch Particles, *Phys. Rev. Lett.* **127**, 108001 (2021).
- [23] S. G. Stuij, H. J. Jonas, Z. Gong, S. Sacanna, T. E. Kodger, P. G. Bolhuis, and P. Schall, Revealing viscoelastic bending relaxation dynamics of isolated semiflexible colloidal polymers, *Soft Matter* **17**, 8291 (2021).
- [24] Z. Gong, T. Hueckel, G. R. Yi, and S. Sacanna, Patchy particles made by colloidal fusion, *Nature (London)* **550**, 234 (2017).
- [25] I. Heller, G. Sitters, O. D. Broekmans, G. Farge, C. Menges, W. Wende, S. W. Hell, E. J. G. Peterman, and G. J. L. Wuite, Sted nanoscopy combined with optical tweezers reveals protein dynamics on densely covered dna, *Nat. Methods* **10**, 910 (2013).
- [26] See Supplemental Material at <http://link.aps.org/supplemental/10.1103/PhysRevMaterials.6.035603> for optical tweezer details concerning rotational freedom of trapped particles and optical tweezer calibration. Additional references used in the Supplemental Material are [27–30].
- [27] A. Stein, S. J. Davidson, J. C. Allegra, and G. F. Allen, Tracer diffusion and shear viscosity for the system 2,6-lutidine-water near the lower critical point, *J. Chem. Phys.* **56**, 6164 (1972).
- [28] G. H. Koenderink, H. Zhang, D. G. A. L. Aarts, M. P. Lettinga, A. P. Philipse, and G. N agele, On the validity of Stokes-Einstein-Debye relations for rotational diffusion in colloidal suspensions, *Faraday Discuss.* **123**, 335 (2003).
- [29] K. C. Neuman and S. M. Block, Optical trapping, *Rev. Sci. Instrum.* **75**, 2787 (2004).
- [30] B. Luki c, S. Jeney,  . Sviben, A. J. Kulik, E.-L. Florin, and L. Forr , Motion of a colloidal particle in an optical trap, *Phys. Rev. E* **76**, 011112 (2007).
- [31] D. Allan, T. Caswell, N. Keim, and C. van der Wel, Trackpy v0.3.1, *Zenodo* **55143** (2016).
- [32] J. W. Hutchinson and W. T. Koiter, Postbuckling theory, *Appl. Mech. Rev.* **23**, 1353 (1970).
- [33] Z. P. Bazant and L. Cedlin, *Stability of Structures* (World Scientific, Singapore, 2009).
- [34] C. Coulais, J. T. B. Overvelde, L. A. Lubbers, K. Bertoldi, and M. van Hecke, Discontinuous Buckling of Wide Beams and Metabeams, *Phys. Rev. Lett.* **115**, 044301 (2015).
- [35] S. Stuij, J. M. van Doorn, T. Kodger, J. Sprakel, C. Coulais, and P. Schall, Stochastic buckling of self-assembled colloidal structures, *Phys. Rev. Research* **1**, 023033 (2019).
- [36] J. R. Gladden, N. Z. Handzy, A. Belmonte, and E. Villermaux, Dynamic Buckling and Fragmentation in Brittle Rods, *Phys. Rev. Lett.* **94**, 035503 (2005).
- [37] J. Chopin, M. Dasgupta, and A. Kudrolli, Dynamic Wrinkling and Strengthening of an Elastic Filament in a Viscous Fluid, *Phys. Rev. Lett.* **119**, 088001 (2017).
- [38] R. Christensen, *Theory of Viscoelasticity: An Introduction* (Elsevier, Amsterdam, 2012).
- [39] H. J. Jonas, S. G. Stuij, P. Schall, and P. G. Bolhuis, A temperature-dependent critical casimir patchy particle model benchmarked onto experiment, *J. Chem. Phys.* **155**, 034902 (2021).